Modulation of the local mass and heat transfer of turbulent double-diffusive convection under stable thermal stratifications

Kenjereš, S.; Roovers, R.

DOI
10.1016/j.ijheatfluidflow.2024.109636

Publication date
2025

Document Version
Final published version

Published in
International Journal of Heat and Fluid Flow

Citation (APA)
Kenjereš, S., & Roovers, R. (2025). Modulation of the local mass and heat transfer of turbulent double-diffusive convection under stable thermal stratifications. *International Journal of Heat and Fluid Flow*, *111*, Article 109636. https://doi.org/10.1016/j.ijheatfluidflow.2024.109636

International Journal of Heat and Fluid Flow 111 (2025) 109636

Contents lists available at ScienceDirect

International Journal of Heat and Fluid Flow

journal homepage: www.elsevier.com/locate/ijhff

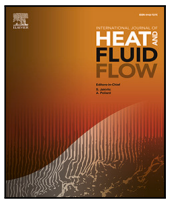

Modulation of the local mass and heat transfer of turbulent double-diffusive convection under stable thermal stratifications

S. Kenjereš [a,b,*], R. Roovers [a]

[a] Transport Phenomena Section, Department of Chemical Engineering, Faculty of Applied Sciences, Delft University of Technology, Van der Maasweg 9, 2629 HZ Delft, The Netherlands

[b] J. M. Burgerscentrum, Research School for Fluid Mechanics, Mekelweg 2, 2628 CD, Delft, The Netherlands

ARTICLE INFO

Keywords:
Double-diffusive convection
Turbulence
Scalar transport
LES
Local mass and heat transfer
Second-order moments

ABSTRACT

We report on numerical studies of bounded double-diffusive turbulent convection, which involves the combined effects of concentration/solutal and thermal buoyancy forces. Our study focuses on an intermediate range of the characteristic non-dimensional numbers, specifically $10^7 \leq Ra_c \leq 10^9$, and $0 \leq Ra_\theta \leq 10^6$. We use fixed values for the concentration and temperature Prandtl numbers (i.e. $Pr_c = 700$, $Pr_\theta = 7$), which approximately correspond to seawater properties. We apply wall-resolved Large Eddy Simulations (LES) and compare the obtained results with available Direct Numerical Simulations (DNS) in the literature. Our findings show an overall good agreement in predicting the global wall mass and heat transfer coefficients, achieved with significantly reduced computational costs. Furthermore, the local mass and heat transfer distributions reveal a high sensitivity to the strength of the vertically imposed stable thermal stratification. Finally, we present the vertical profiles of the long-term time-averaged first and second moments.

1. Introduction

The combined effects of thermal and concentration buoyancy (double-diffusive convection) play an important role in various environmental (mixing in the upper layer of oceans), astrophysical (helium-core stars), and industrial (solar ponds, blast furnaces, energy storage tanks) applications, e.g. Turner (1974, 1985), Huppert and Turner (1981), Hanjalić and Musemić (1997), Zaussinger and Kupka (2019), Yang et al. (2016a,b), Chakkingal et al. (2020) and Zuo et al. (2024).

The importance of double-diffusive convection phenomena in oceanography was recognized in a series of pioneering works by Turner (1974), Huppert and Turner (1981) and Turner (1985), who covered a detailed overview of theoretical and laboratory-scale experimental studies in the literature. In addition, relatively simple theories addressing the stability criteria of double-diffusive convection were proposed. More recently, high Rayleigh number convection with double-diffusive fingers, which represent a typical morphology of the concentration field, was experimentally investigated by Hage and Tilgner (2010). To achieve a sufficiently high ratio of concentration and thermal diffusion, the authors applied an electrochemical system where the ion concentration of the working electrolyte (a solution of $CuSO_4$ in H_2SO_4) imposed destabilizing effects, while temperature played a stabilizing role. The different heights of the experimental cell enabled exploration of a wide range of working parameters (i.e. $10^{10} \leq Ra_c \leq 10^{12}$). Thanks to the fluid transparency, the Particle Image Velocimetry (PIV) measurements were performed to provide a detailed velocity field in the vertical cross-section. The typical finger-like structures were generated within the range of working parameters considered, and scaling laws for the integral mass transfer and finger thickness were proposed. In the follow-up experimental study of Kellner and Tilgner (2014), with an identical electrochemical system as used in Hage and Tilgner (2010), the transition between convective cells and finger regimes was investigated. Finally, in Rosenthal et al. (2022), the concentration Rayleigh number range was increased even further (up to $Ra_c = 10^{14}$), and changes in the morphology of the flow and concentration fields were analysed. The formation of the double-diffusive staircases was observed even under unstable density stratification conditions.

In a series of direct numerical simulations (DNS) studies on vertically bounded double-diffusive configuration, the salinity transfer over a range of working parameters and different aspect ratios of the computational domain was investigated by Yang et al. (2015, 2016a) and Yang et al. (2016b). The scaling laws for the concentration mass transfer were found to match well with the classical GL theory, Grossmann and Lohse (2000). Furthermore, a transition from typical Rayleigh–Bénard cells to finger-structures was analysed.

* Corresponding author at: Transport Phenomena Section, Department of Chemical Engineering, Faculty of Applied Sciences, Delft University of Technology, Van der Maasweg 9, 2629 HZ Delft, The Netherlands.
E-mail address: s.kenjeres@tudelft.nl (S. Kenjereš).

https://doi.org/10.1016/j.ijheatfluidflow.2024.109636
Received 8 May 2024; Received in revised form 21 August 2024; Accepted 29 October 2024
Available online 21 November 2024

Nomenclature

D_c^m	Molecular concentration diffusion coefficient (m^2/s)
D_θ^m	Molecular temperature diffusion coefficient (m^2/s)
Nu_θ	Thermal Nusselt number (–)
Nu_c	Concentration Nusselt number (–)
Pr_θ	Thermal Prandtl number (–)
Pr_c	Concentration Prandtl number (–)
Ra_θ	Temperature Rayleigh number (–)
Ra_c	Concentration Rayleigh number (–)
c	Concentration (kg/m^3)
f_i	External force per unit fluid volume (N/m^3)
g_i	Gravity (m/s^2)
p	Pressure (Pa)
u_i	Velocity vector (m/s)
D	Domain depth (in the y-direction) (m)
H	Domain height (in the vertical z-direction) (m)
L	Domain length (in the horizontal x-direction) (m)

Greek Symbols

β_θ	Thermal expansion coefficient (1/K)
β_c	Concentration expansion coefficient (m^3/kg)
ν	Kinematic viscosity (m^2/s)
ν_t^{sgs}	Turbulent subgrid kinematic viscosity (m^2/s)
ρ_0	Density (kg/m^3)
$\tau_{\theta j}^{sgs}$	Subgrid turbulent heat flux vector (m K/s)
τ_{cj}^{sgs}	Subgrid turbulent concentration flux vector (m^2 kg/s)
τ_{ij}^{sgs}	Subgrid turbulence stress tensor (m^2/s^2)
θ	Temperature (K)

Other symbols and Abbreviations

DNS	Direct Numerical Simulation
LES	Large Eddy Simulation
MPI	Message Passing Interface

Subscripts

i, j	Vector index

In the present study, similarly as in Yang et al. (2016b), we focus on a situation typical for the ocean's upper layer, where the concentration gradient is the main driving mechanism to initiate mixing, while the temperature gradient plays a suppressing role. Due to the high values of characteristic Prandtl numbers (i.e. thermal $Pr_\theta = O(10)$, and concentration $Pr_c = O(10^2)$), we adopt the wall-resolving Large-Eddy Simulation (LES) approach to make numerical simulation costs acceptable. This approach proved to work very well in simulations of the natural convection (pure thermal buoyancy driven flows), as shown in studies by Kenjereš and Hanjalić (2006) and Kenjereš (2015), in flows subjected to the combined effects of electromagnetic forcing and thermal buoyancy for electrolyte fluids ($Pr_\theta = O(10)$), as demonstrated by Kenjereš (2008, 2009) and Kenjereš (2011), and in mass transfer of a high Schmidt number ($Sc = Pr_c = O(10^3)$) fluid in a flow within a complex foam-like porous structure, as described by Zenklusen et al. (2016). For all the above-mentioned applications of the wall-resolving LES, very good agreement was obtained with the fully resolving DNS, as well as the combined particle image velocimetry and laser-induced fluorescence (PIV/LIF) measurements.

The main goals of the present study are: (i) to determine the agreement between the proposed wall-resolving LES and fully resolving DNS of Yang et al. (2015, 2016b) over a range of working parameters, (ii) to provide the local mass and heat transfer distributions along the active boundaries, and, (iii) to provide profiles of the long-term time-averaged second-moments (i.e. temperature and concentration variances, turbulent kinetic energy, as well as the turbulent mass and heat flux correlations).

Note that, at present, information addressing above-listed goals (ii) and (iii) is either scarce or totally missing in the literature, but is crucially important for the further development, testing, and validation of Reynolds-Averaged Navier–Stokes (RANS) type models for double-diffusive convection in the turbulent flow regimes, as pointed out by Hanjalić and Musemić (1997).

2. Numerical simulations

2.1. Mathematical model

The transport of mass, momentum, heat and species in the double diffusive convection in a turbulent regime is defined by the following spatially-averaged transport equations used in the Large Eddy Simulation (LES) approach, and can be written as:

$$\frac{\partial u_i}{\partial x_i} = 0 \tag{1}$$

$$\frac{\partial u_i}{\partial t} + \frac{\partial (u_i u_j)}{\partial x_j} = \frac{\partial}{\partial x_j}\left[\nu\left(\frac{\partial u_i}{\partial x_j} + \frac{\partial u_j}{\partial x_i}\right) - \tau_{ij}^{sgs}\right] + \frac{1}{\rho_0} f_i \tag{2}$$

$$\frac{\partial c}{\partial t} + \frac{\partial (c u_j)}{\partial x_j} = \frac{\partial}{\partial x_j}\left(D_c^m \frac{\partial c}{\partial x_j} - \tau_{cj}^{sgs}\right) \tag{3}$$

$$\frac{\partial \theta}{\partial t} + \frac{\partial (\theta u_j)}{\partial x_j} = \frac{\partial}{\partial x_j}\left(D_\theta^m \frac{\partial \theta}{\partial x_j} - \tau_{\theta j}^{sgs}\right) \tag{4}$$

where ρ_0 is density of fluid at reference temperature (θ_0) and concentration (c_0), D_θ^m is molecular thermal diffusion ($D_\theta^m = \nu/Pr_\theta$), D_c^m is molecular concentration diffusion ($D_c^m = \nu/Pr_c$) f_i represents body forces (per fluid unit volume) acting on the fluid, and, finally, τ_{ij}^{sgs}, τ_{cj}^{sgs}, $\tau_{\theta j}^{sgs}$ are subgrid turbulent stress tensor, concentration flux, and thermal flux, respectively, that need to be modelled. For the double-diffusive convection, the pressure and gravitational forces need to be included, where for the latter, the Boussinesq approximation is applied for both thermal and concentration buoyancy terms:

$$f_i^p = -\frac{\partial (p - p_0)}{\partial x_i}, \quad f_i^g = -g_i\left[\beta_\theta\left(\theta - \theta_0\right) - \beta_c\left(c - c_0\right)\right] \tag{5}$$

where

$$\beta_\theta = -\frac{1}{\rho_0}\left(\frac{\partial \rho}{\partial \theta}\right)_{p_0,\rho_0,c_0}, \quad \beta_c = \frac{1}{\rho_0}\left(\frac{\partial \rho}{\partial c}\right)_{p_0,\rho_0,\theta_0} \tag{6}$$

are thermal and concentration expansion coefficients, respectively, and p_0 is reference pressure.

In the present work, we adopt the subgrid closure of Vreman (2004), which was tested over a range of turbulent shear flows and found to be as good as a dynamic Smagorinsky model, but was more numerically efficient. Additionally, this SGS model proved to work well for the pure turbulent thermal-buoyancy driven flows too, as shown in Kenjereš (2015):

$$\tau_{ij}^{sgs} = -\nu_t^{sgs}\left(\frac{\partial u_i}{\partial x_j} + \frac{\partial u_j}{\partial x_i}\right) + \frac{1}{3}\tau_{kk}^{sgs}\delta_{ij} \tag{7}$$

$$\nu_t^{sgs} = C^{sgs}\sqrt{\frac{B_\beta}{\alpha_{ij}\alpha_{ij}}}, \quad \alpha_{ij} = \frac{\partial u_i}{\partial x_j}, \quad \beta_{ij} = \Delta_m^2 \alpha_{mi}\alpha_{mj},$$

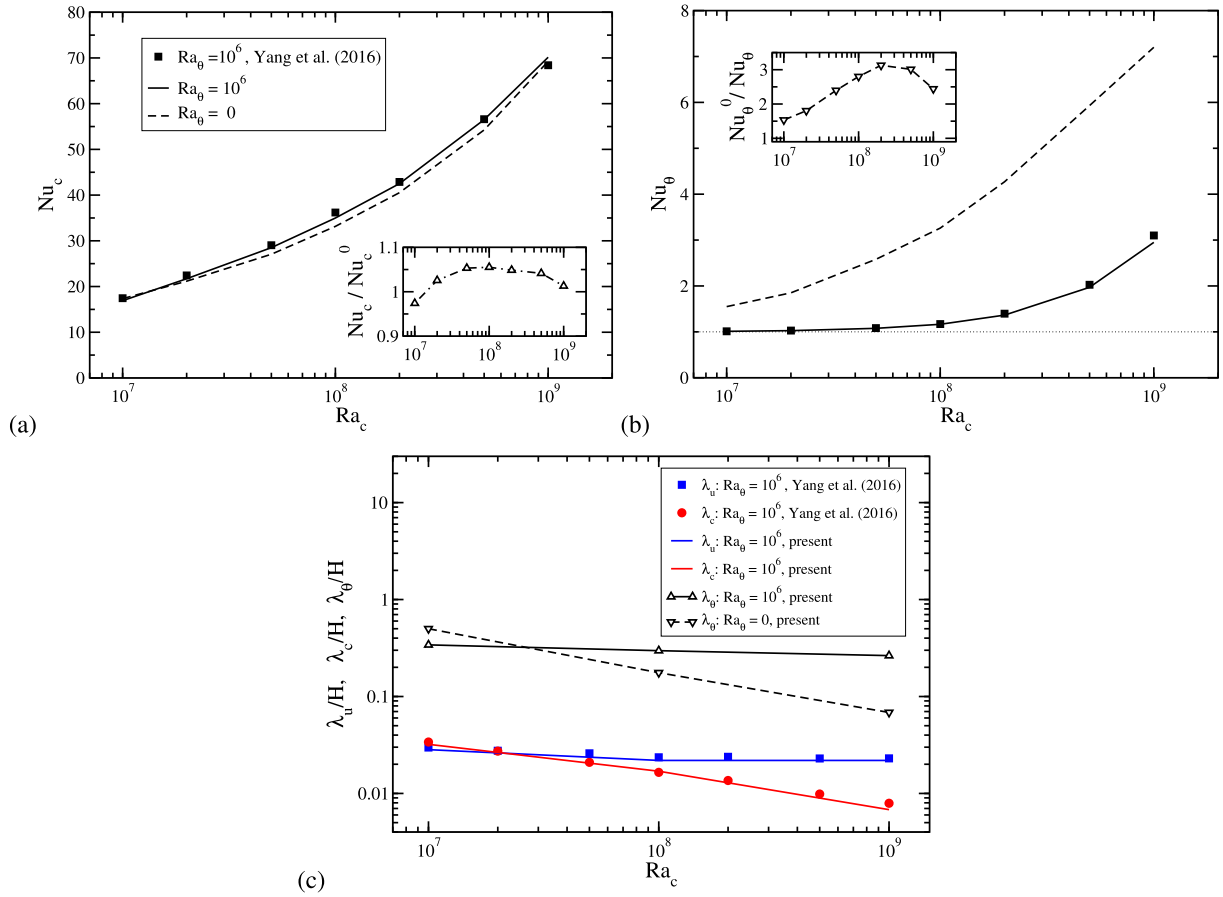

Fig. 1. Dependency of the integral concentration Nusselt number (Nu_c) (a) and temperature Nusselt number (Nu_θ) (b) over the range of $10^7 \leq Ra_c \leq 10^9$ for two values of $Ra_\theta = 0$ and 10^6. For the latter, the present results are compared with DNS of Yang et al. (2016a). Note that zoom-ins show a ratio of the integral concentration Nusselt (Nu_c/Nu_c^0) (a) and integral temperature Nusselt (Nu_θ^0/Nu_θ) (b) numbers, where Nu_c^0 and Nu_θ^0 are values for the neutral case. Thickness of the momentum (λ_u) (–), concentration (λ_c) (–), and temperature (λ_θ) (–) boundary layers (c). The first two are compared with reported values of Yang et al. (2016a) for $Ra_\theta = 10^6$. Furthermore, for the present simulations, the impact of the Ra_θ on thickness of the temperature boundary layer is shown, (λ_θ) (––) at $Ra_\theta = 0$, and (–) at $Ra_\theta = 10^6$. Note that graphs (a) and (b) are shown in the semi-log scale, whereas graph (c) is in the log–log scale.

$$B_\beta = \beta_{11}\beta_{22} - \beta_{12}^2 + \beta_{11}\beta_{33} - \beta_{13}^2 + \beta_{22}\beta_{33} - \beta_{23}^2 \tag{8}$$

with a model coefficient $C^{sgs} = 0.07$, and the control volume filter-length projections Δ_m. The subgrid turbulent concentration and heat fluxes are modelled by a simple-gradient diffusion hypothesis (SGDH):

$$\tau_{cj}^{sgs} = -\frac{\nu_t^{sgs}}{Pr_c^{sgs}}\frac{\partial c}{\partial x_j}, \quad \tau_{\theta j}^{sgs} = -\frac{\nu_t^{sgs}}{Pr_\theta^{sgs}}\frac{\partial \theta}{\partial x_j}, \tag{9}$$

with the adopted values of the subgrid turbulent Prandtl numbers of $Pr_c^{sgs} = 0.7$ and $Pr_\theta^{sgs} = 0.4$. The former value is based on the large eddy simulations of the mixing of a passive scalar in a high-Schmidt turbulent jet presented in Mejia et al. (2015), while the latter is based on previous LES studies of the pure thermal-buoyancy convection over a range of Rayleigh numbers, Eidson (1984) and Kenjereš (2015).

The double diffusion phenomenon is determined by the following set of the characteristic non-dimensional parameters: $Ra_c, Pr_c, Ra_\theta, Pr_\theta$. The characteristic thermal and concentration Rayleigh numbers are defined as:

$$Ra_\theta = \beta_\theta\, g\, \Delta\theta\, Pr_\theta\, \frac{H^3}{\nu^2}, \quad Ra_c = \beta_c\, g\, \Delta c\, Pr_c\, \frac{H^3}{\nu^2} \tag{10}$$

where $\Delta\theta = (\theta_{top} - \theta_{bottom})$, and $\Delta c = (c_{top} - c_{bottom})$, where subscripts indicate the boundaries of the domain at which temperature and concentration are imposed. In addition, the characteristic density ratio can be introduced:

$$\Lambda = \frac{Ra_\theta}{Ra_c} \cdot Le = \frac{Ra_\theta}{Ra_c} \cdot \frac{Pr_c}{Pr_\theta} = \frac{\beta_\theta \Delta\theta}{\beta_c \Delta c} \tag{11}$$

where Le is the Lewis number. In the present study we adopt $Pr_c = 700$ and $Pr_\theta = 7$ (that gives a fixed value of $Le = 100$), which corresponds to seawater properties at 20 °C. We focus on an intermediate range of working parameters, i.e. $10^7 \leq Ra_c \leq 10^9$, and $Ra_\theta = 0, 10^6$ (where $Ra_\theta = 0$ indicates a passive scalar behaviour of temperature, whereas $Ra_\theta = 10^6$ indicates a strong stable thermal stratification level). This gives the following range of the characteristic density ratio of $0 \leq \Lambda \leq 10$ at $Ra_c = 10^7$, $0 \leq \Lambda \leq 1$ at $Ra_c = 10^8$, and $0 \leq \Lambda \leq 0.1$ at $Ra_c = 10^9$, respectively.

2.2. Numerical method

We solve the discretized forms of the above-defined governing PDE equations (Eqs. (1)–(4)) using our in-house finite-volume code for general non-orthogonal structured geometries. The code has been extensively validated and applied in our previous work, where we addressed various cases of turbulent heat transfer simulations within the LES modelling framework, e.g. Kenjereš and Hanjalić (2006) and Kenjereš (2015). The collocated grid arrangement is applied for all transport variables, and Cartesian vector and tensor components are used. The Rhie–Chow interpolation method is employed to prevent decoupling between the pressure and velocity fields, Ferziger et al. (2019). The linear system of equations is solved by the strongly implicit procedure (SIP) developed by Stone (1968) and further discussed in Ferziger et al. (2019). The SIMPLE algorithm is used to solve the pressure field, Patankar (1980). The code achieves the second-order numerical accuracy. Both the convective and diffusive terms of

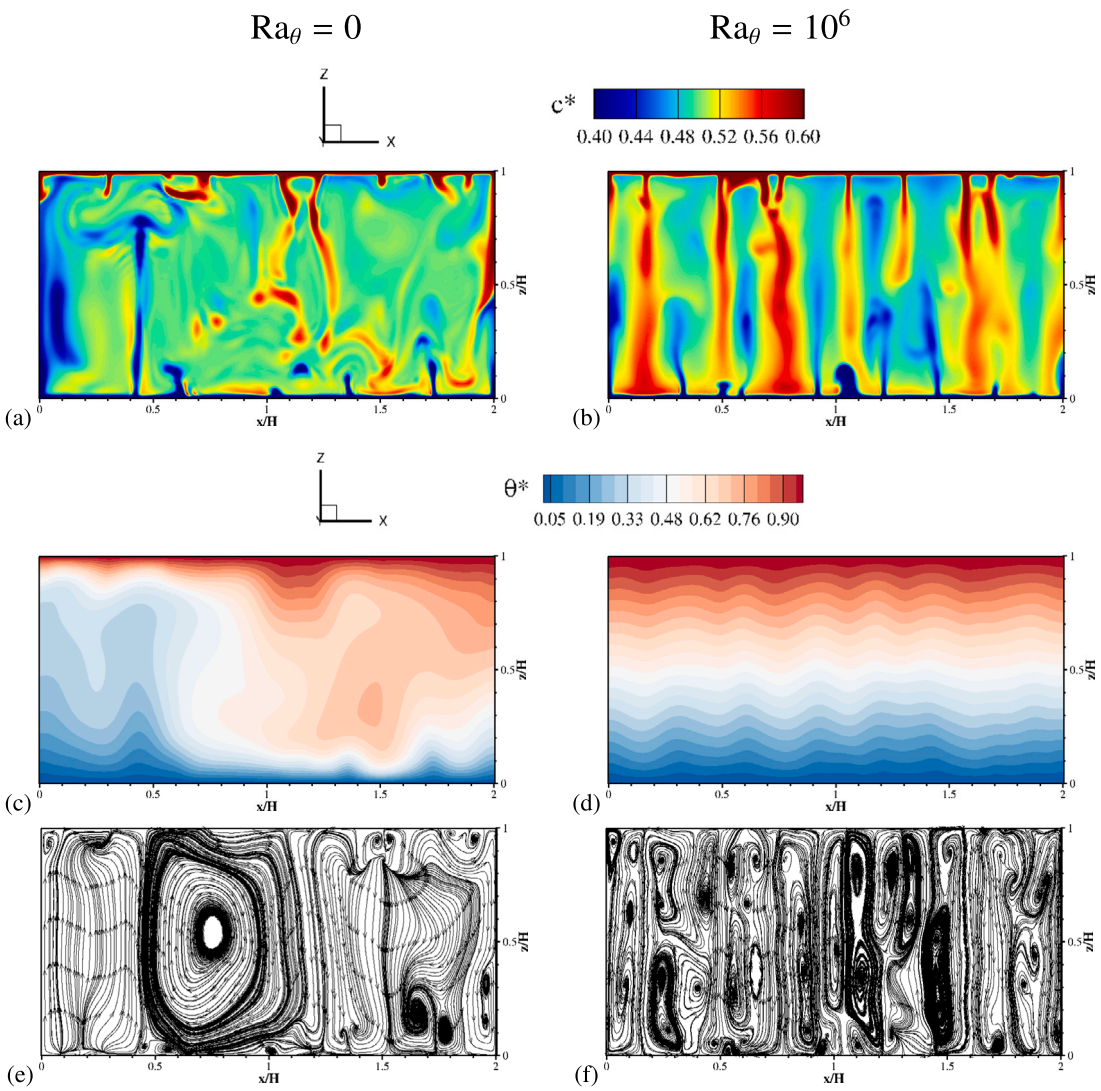

Fig. 2. Contours of the instantaneous non-dimensional concentration ($c^*=c/\Delta c$), temperature ($\theta^*=\theta/\Delta\theta$), and streamlines in the central vertical plane (y/D = 0.5), for $Ra_c = 10^8$, and two values of $Ra_\theta = 0$ (-left), and $Ra_\theta = 10^6$ (-right).

all transport equations are calculated using the central-differencing scheme (CDS). Fully implicit time integration is performed using the three-time-level scheme. The finite-volume numerical code is designed for efficient parallel execution by employing 3D domain decomposition and message passing interface (MPI) directives, Kenjereš (2015).

2.3. Geometry, boundary conditions and numerical mesh

We consider a simple rectangular computational domain with the $L_x : L_y : L_z = L : D : H = 2 : 2 : 1$ aspect ratio, where the upper surface was kept at a constant high temperature (θ_{top}) and concentration (c_{top}), while the lower surface was kept at constant low temperature (θ_{bottom}) and concentration (c_{bottom}). To make an analogy with practical applications, this configuration represents a situation where a warmer and saltier layer initially resides above the colder and less salty layer of the fluid. Gravity acts in the negative vertical direction (i.e. $g_i(0,0,-1)$), so the imposed concentration gradient tends to promote mixing, while the temperature gradient tends to stabilize the flow due to stable thermal stratification. For the upper and lower horizontal boundaries, a no-slip condition is applied for the velocity ($u_i = 0$). All side-boundaries are treated as a free-slip for velocity and zero-gradient fluxes for temperature and concentration, respectively. We apply a non-uniform numerical mesh with $N_x \times N_y \times N_z = 256 \times 256 \times 162$ control volumes. To properly resolve steep concentration and temperature gradients in the proximity of the horizontal walls, and to have an adequate mesh in the central part of the domain, we apply a non-uniform mesh distribution in the vertical direction, and a uniform distribution in both horizontal directions. We split the vertical direction in three segments: (i) $0 \le z/H \le 0.05$, (ii) $0.05 < z/H < 0.95$, and (iii) $0.95 \le z/H \le 1$. Segments near the walls are refined such that the first control volumes attached to the walls have $\Delta z^*_{wall} = \Delta z_{wall}/H = 5 \times 10^{-5}$, and the remaining 30 control volumes (per segment) gradually increase with a grid-expansion ratio of 1.1. This refinement is done in order to properly resolve thin concentration boundary layers even at the highest value of $Ra_c = 10^9$, with thickness estimated from $\delta_c = 1/2\ H\ Nu_c^{-1}$, Yang et al. (2016a). The central segment has a uniform distribution that is adequate to properly capture the thickness of the emerging concentration and thermal plumes. As initial conditions, the velocity field is assumed to be zero, while the temperature and concentration fields are assumed to be uniform and equal to corresponding reference values, i.e. $\theta_0 = \left(\theta_{top} + \theta_{bottom}\right)/2, c_0 = \left(c_{top} + c_{bottom}\right)/2$, respectively.

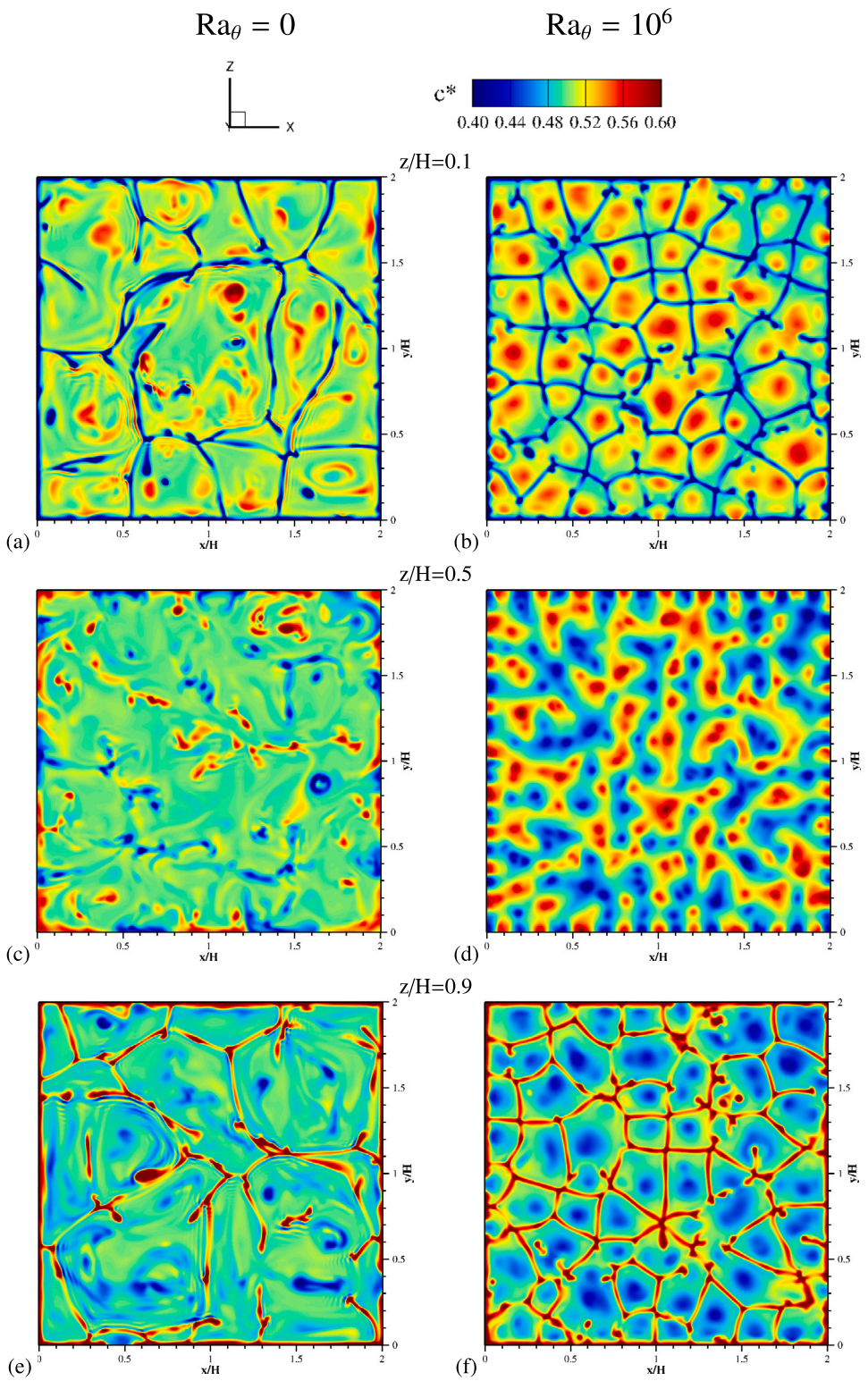

Fig. 3. Contours of the instantaneous non-dimensional concentration ($c^*=c/\Delta c$) in three horizontal planes (z/H = 0.1, 0.5, 0.9) (from top to bottom) for $Ra_c = 10^8$ and $Ra_\theta = 0$ (-left), $Ra_\theta = 10^6$ (-right). (For interpretation of the references to colour in this figure legend, the reader is referred to the web version of this article.)

3. Results and discussion

3.1. Integral mass and heat transfer, boundary layers

We start our analysis by comparing the present results with the DNS of Yang et al. (2016a), as shown in Fig. 1. The DNS results by Yang et al. (2016a) were obtained using an originally developed dual-mesh approach with a finite-difference code with a staggered mesh arrangement (Ostilla-Mónico et al., 2015) where different meshes were applied for the velocity (288^3) and scalar (864^3) fields, at $Ra_c = 10^9$, $Ra_\theta = 10^6$. As mentioned above, the present simulations are based on a single non-uniform mesh for all transport variables and all simulations. This approach enabled the numerically efficient development of momentum and scalar fields at higher Ra_c by initializing all fields

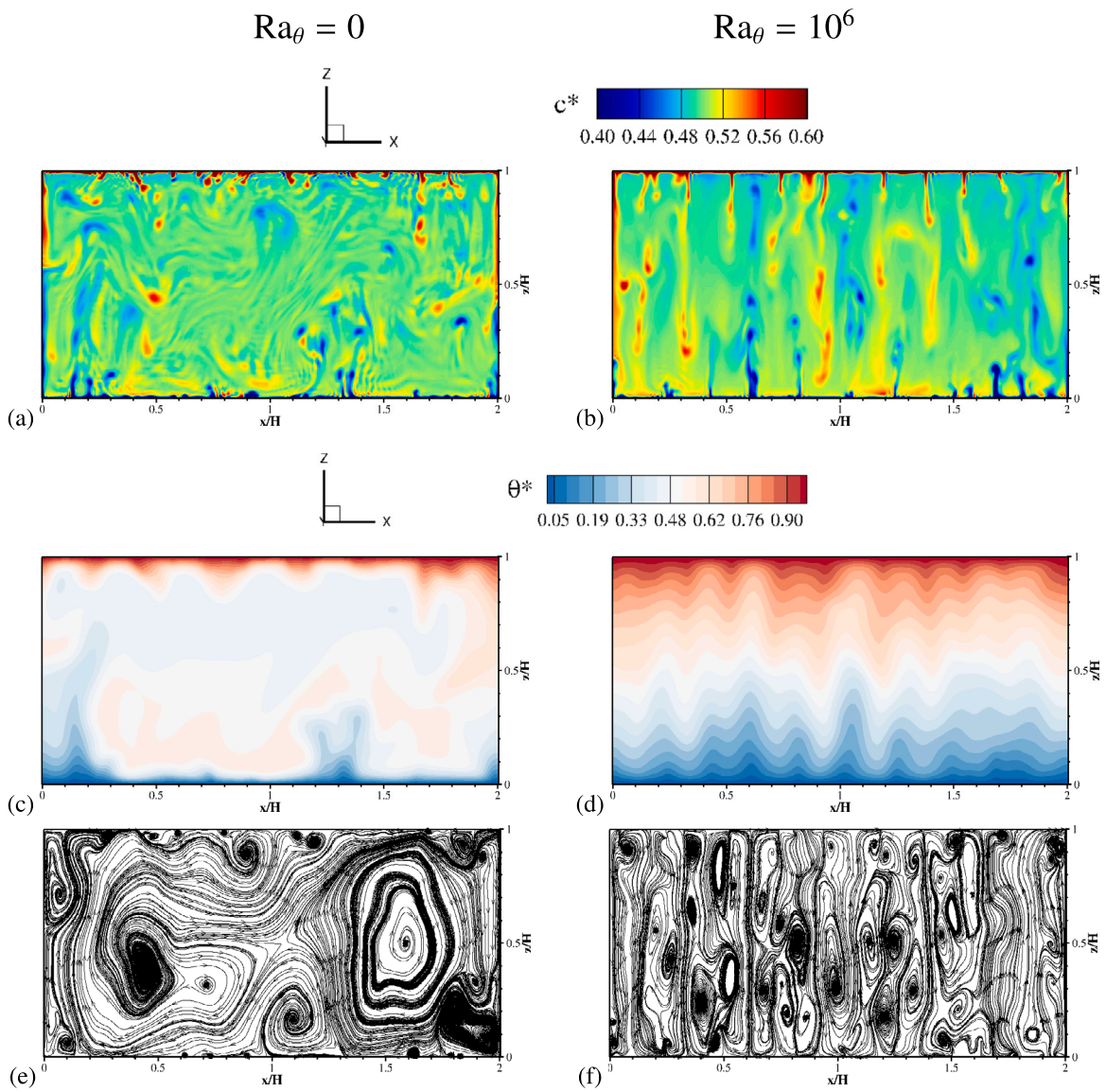

Fig. 4. Contours of the instantaneous non-dimensional concentration (c/c_0), temperature (θ/θ_0), and streamlines in the central vertical plane ($y/D = 0.5$), for $Ra_c = 10^9$, and two values of $Ra_\theta = 0$ (-left), and 10^6 (-right).

from fully developed and statistically convergent solutions obtained at lower Ra_c. It can be seen that a good agreement between the present simulation and DNS results of Yang et al. (2016a) (both performed at $Ra_\theta = 10^6$) is obtained for both Nu_c (Fig. 1(a)) and Nu_θ (Fig. 1(b)) over the entire range of simulated Ra_c.

Note that the local instantaneous concentration and temperature Nusselt numbers at the active walls are calculated as: $Nu'_c(x,y,t) = (\partial c/\partial z)|_{wall} \cdot H/\Delta c$ and $Nu'_\theta(x,y,t) = (\partial\theta/\partial z)|_{wall} \cdot H/\Delta\theta$, whereas their integral mean values are evaluated as: $Nu_c = 1/T_0 \int_{t=0}^{T_0} \left(1/L \cdot 1/D \int_{\Delta x}\int_{\Delta y} Nu'_c dxdy\right) dt$ and $Nu_\theta = 1/T_0 \int_{t=0}^{T_0} \left(1/L \cdot 1/D \int_{\Delta x}\int_{\Delta y} Nu'_\theta dxdy\right) dt$, where T_0 is the period of time-integration. The largest deviation, a 2.5% difference in Nu_θ, was observed at $Ra_c = 10^9$. This can be partially explained by: (i) changes in the aspect ratio of DNS, where the reduced geometry (1:1:0.8) was simulated with periodic-boundary conditions, while we kept the original (2:2:1) aspect ratio in all simulations, and (ii) significantly longer interval of collecting statistics in our simulations (10 times longer) compared to the DNS.

Next, we focus on the importance of subgrid turbulence contributions, particularly concerning the concentration field, due to the relatively large value of the corresponding concentration Prandtl number. Note that for fully resolving DNS, the critical parameter is the Batchelor length scale for the concentration field, defined as $\eta_B = \eta_K/Pr_c^{1/2}$, where $\eta_K = (\nu^3/\varepsilon)^{1/4}$ is the Kolmogorov length scale, and ε is dissipation rate of the turbulent kinetic energy. To quantify the subgrid turbulent concentration flux contribution, we analyse the ratio of turbulent ($D_c^{sgs} = \nu_t^{sgs}/Pr_c^{sgs}$) to molecular diffusivities ($D_c^m = \nu/Pr_c$), i.e. D_c^{sgs}/D_c^m, for the simulations performed. The time-evolution of the maximum of this ratio, when a fully developed and statistically convergent flow, heat, and mass transfer are established, is shown in Fig. A.10. It can be seen that this ratio is larger for the neutral (i.e. when $Ra_\theta = 0$) than for the strong-stratification cases ($Ra_\theta = 10^6$) for the considered values of Ra_c. Furthermore, at $Ra_c = 10^7$, we observe that $D_c^{sgs}/D_c^m \ll 1$, indicating that the simulations are practically fully resolving. In contrast, at $Ra_c = 10^9$, the turbulent subgrid concentration contributions dominate over the molecular ones, while at $Ra_c = 10^8$, both turbulent and molecular contributions are of similar importance. For these cases, we satisfy the criterion for a well-resolved LES as defined in Celik et al. (2005). The local distribution of the characteristic ratio in the central vertical plane at an arbitrary time instant is shown in

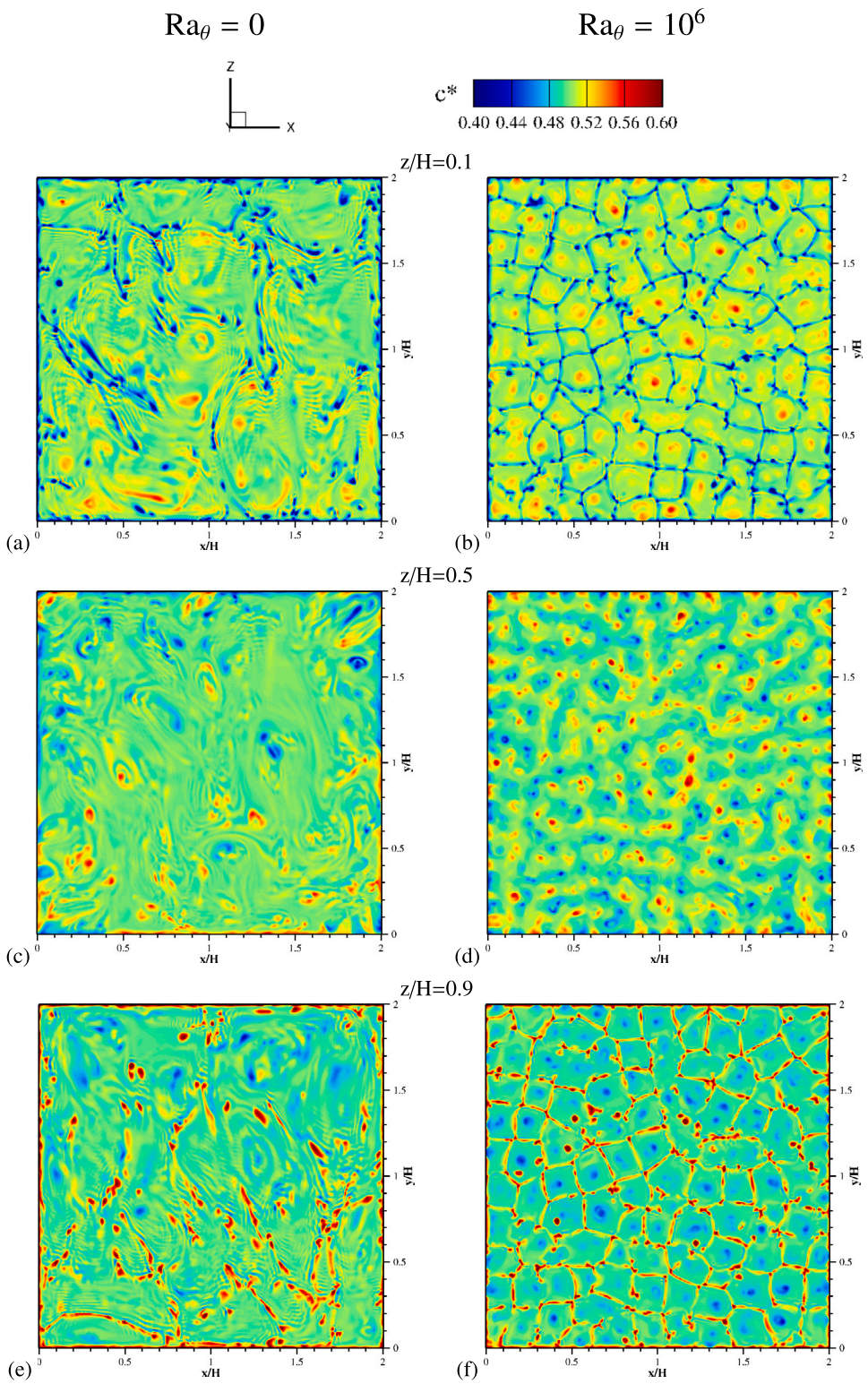

Fig. 5. Contours of the instantaneous non-dimensional concentration ($c^*=c/\Delta c$) in three horizontal planes (z/H = 0.1, 0.5, 0.9) (from top to bottom) for $Ra_c = 10^9$ and $Ra_\theta = 0$ (-left), $Ra_\theta = 10^6$ (-right). (For interpretation of the references to colour in this figure legend, the reader is referred to the web version of this article.)

Figs. A.11 and A.12. The contours of the characteristic diffusivities ratio indicate that the regions in the vicinity of the active boundaries are well resolved (i.e. we have a wall-resolved LES), and that the turbulent subgrid contributions are dominant in the central part of the domain.

By comparing the characteristic momentum (λ_u) and concentration (λ_c) boundary layer thicknesses, defined as the location where the corresponding root mean square (r.m.s.) values of the instantaneous horizontal velocity ($\sqrt{\overline{u'^2_{x,y}}}$) and concentration ($\sqrt{\overline{c'}}$) reach their maximum, we can conclude that there is an overall good agreement between the reference DNS of Yang et al. (2016a) and the present work, as shown in Fig. 1(c). It can be seen that the concentration boundary layers becomes progressively thinner with increasing Ra_c.

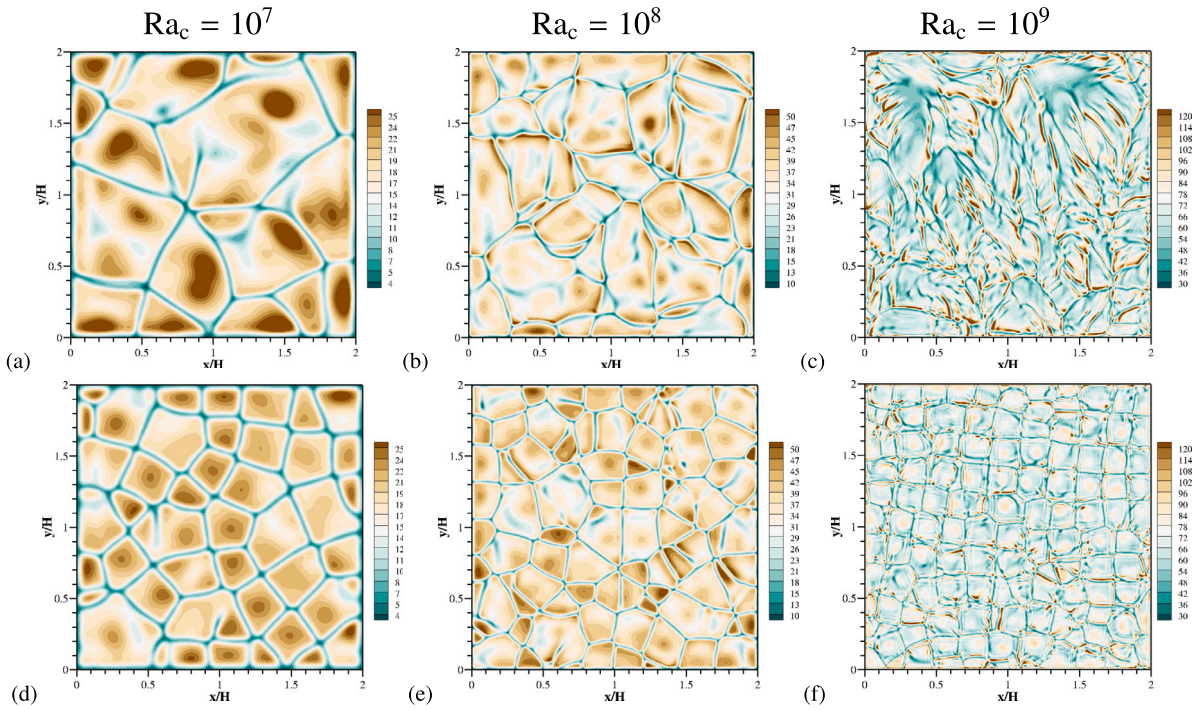

Fig. 6. Contours of the instantaneous local concentration Nusselt number (Nu_c') at the upper wall for different values of $Ra_c = 10^7, 10^8, 10^9$ and $Ra_\theta = 0$ (-top), $Ra_\theta = 10^6$ (-bottom).

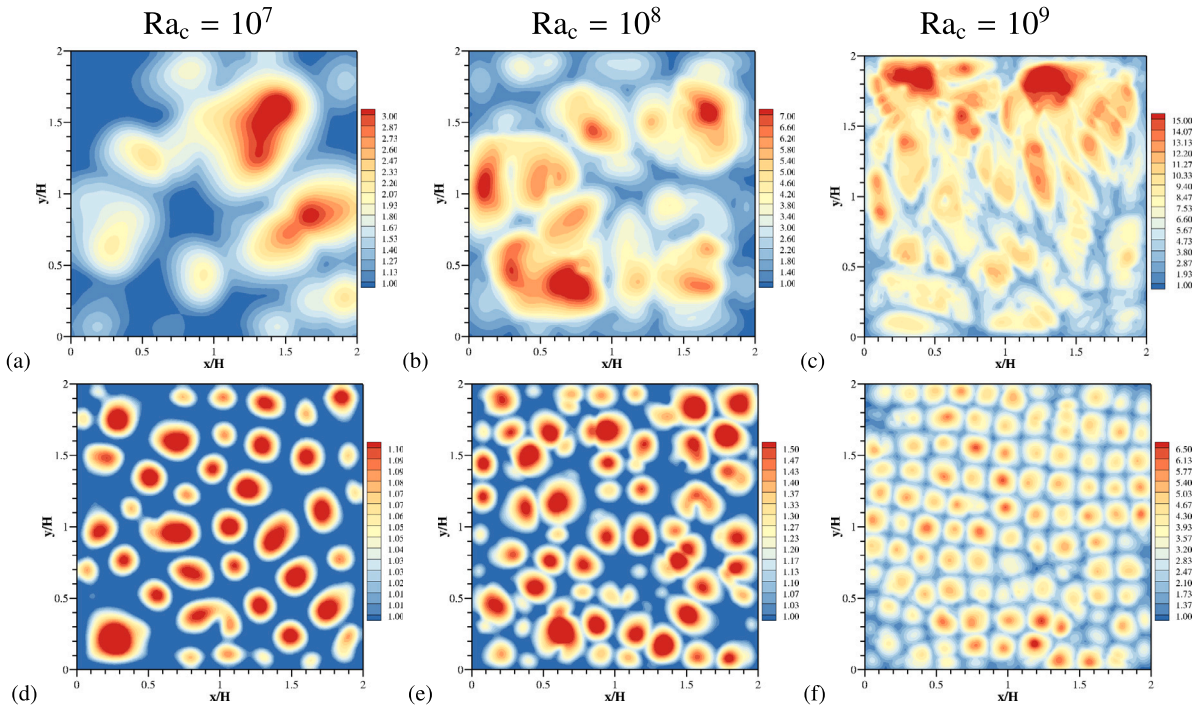

Fig. 7. Contours of the instantaneous local temperature Nusselt number (Nu_θ') at the upper wall for different values of $Ra_c = 10^7, 10^8, 10^9$ and $Ra_\theta = 0$ (-top), $Ra_\theta = 10^6$ (-bottom).

This behaviour was also observed earlier in pure natural convection over an extensive range of temperature Rayleigh numbers for fluids with a temperature Prandtl number close to one, Zhou and Xia (2001) and Kenjereš and Hanjalić (2002). In contrast, for the velocity boundary layer, after an initial reduction, a constant value is observed, as shown in Fig. 1(c). A similar behaviour is also observed for the temperature boundary layer (λ_θ), which is analogous to the concentration scalar, defined as a location where ($\sqrt{\overline{\theta'}}$) reaches its maximum. For higher values of $Ra_c \geq 5 \times 10^7$, the concentration boundary layer is nested within the velocity boundary layer. Both layers are always deeply nested within the temperature boundary layer. Note that this behaviour of the boundary layers is different from typical forced convection flows, where both the temperature and concentration boundary layers will be embedded within the velocity boundary layer.

Next, we take a step back and analyse the differences between the neutral temperature field ($Ra_\theta = 0$) and strong temperature stratification ($Ra_\theta = 10^6$) cases, as indicated by dashed and solid lines in Fig. 1, respectively. An interesting conclusion can be drawn by

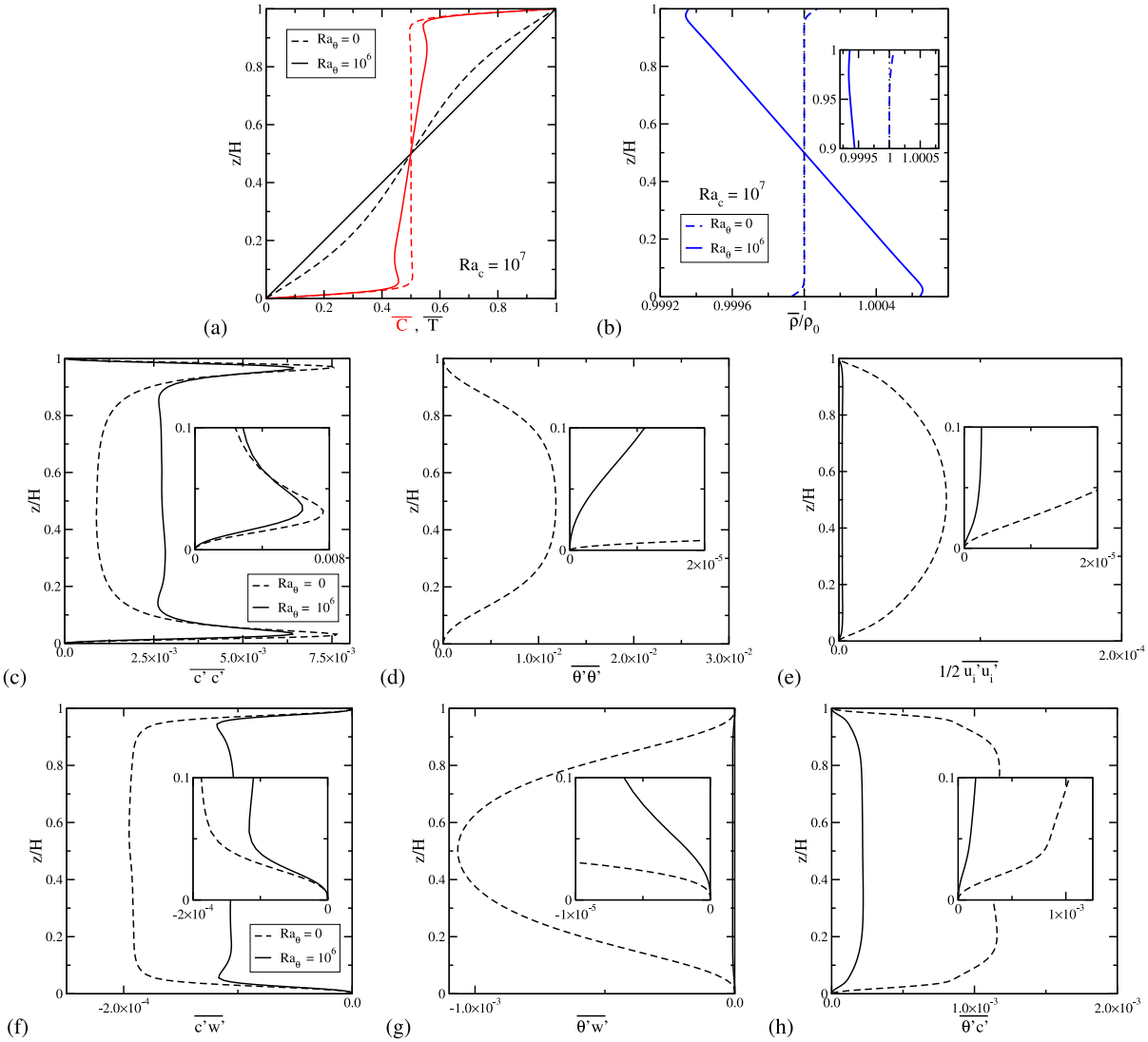

Fig. 8. Vertical profiles of the mean concentration ($\overline{C}$), temperature ($\overline{T}$), density ($\overline{\rho}$), and second-order moments at $Ra_c = 10^7$ and two values of $Ra_\theta = 0$ (-dashed line) and 10^6 (-solid line) and with a zoom-in in the proximity of the lower horizontal wall ($0 \le z/H \le 0.1$). Note that the (cross)correlations involving the velocity were non-dimensionalized with the free–fall concentration buoyancy velocity ($U_0 = \sqrt{\beta_c g \Delta c H}$).

comparing Fig. 1(a) and (b). There is a suppression of the Nu_θ with Ra_θ increase, Fig. 1(b), The strongest suppression ($Nu_\theta^0/Nu_\theta \approx 3$) is obtained at $Ra_\theta = 2 \times 10^8$, as seen in zoom-in of Fig. 1(b). The opposite trend is obtained for the mass transfer, where Nu_c is slightly increased (where the maximum enhancement of $Nu_c/Nu_c^0 = 1.055$ occurring at $Ra_c = 10^8$, see zoom-in of Fig. 1(a)). A similar observation of mass transfer increase with an increase in Ra_θ was reported in Yang et al. (2016b). By comparing the thickness of the thermal boundary layers, it can be seen that a significantly faster thinning is obtained for the neutral case, while for the $Ra_\theta = 10^6$, there is just a marginal variation, Fig. 1(c). There is a cross-over at approximately $Ra_c = 3 \times 10^7$. From the integral mass and heat transfer distributions, as well as from the behaviour of typical boundary layers, it can be concluded that the present simulations provide reliable results in a good agreement with the fully scalar-resolving DNS of Yang et al. (2016a).

3.2. Instantaneous flow, concentration and temperature fields

Contours of the instantaneous non-dimensional concentration, temperature, and velocity fields at different values of Ra_c and Ra_θ are shown in Figs. 2–5. We first select the intermediate value of $Ra_c = 10^8$. The contours of concentration and streamline plots in the central vertical cross-section for $Ra_\theta = 0$ reveal a typical flow morphology consisting of large coherent convective structures generated by strong vertical shear originating from the updrafts and downdrafts of the concentration field, as seen in Fig. 2(a-c-e). This is in accordance with the classical case of the Rayleigh–Bénard convection, except that we are dealing with driving concentration buoyancy effects, and temperature field acts as a passive scalar (by setting $\beta_\theta = 0$). The temperature field distribution is characterized by significantly larger structures (thermal plumes) in comparison to the concentration field.

After the activation of thermal buoyancy effects at $Ra_\theta = 10^6$, significant flow reorganization occurs, Fig. 2(b-d-f). Due to the suppressing effects of the imposed temperature gradient, the size of convective structures is significantly reduced in the horizontal direction, resulting in a larger number of rolls, as seen in Fig. 2(f). It is interesting to note that a similar flow reorganization occurs in Rayleigh–Bénard convection when subjected to a strong vertical magnetic field, as reported in Kenjereš and Hanjalić (2004). The distinct structure of the concentration plumes (so-called salt or concentration fingers) extends through the entire vertical cross-section with impinging regions on the opposite walls, as shown in Fig. 2(b). This transition from convective cell structures to concentration fingers is in good agreement with the experimental studies of Kellner and Tilgner (2014) and the numerical

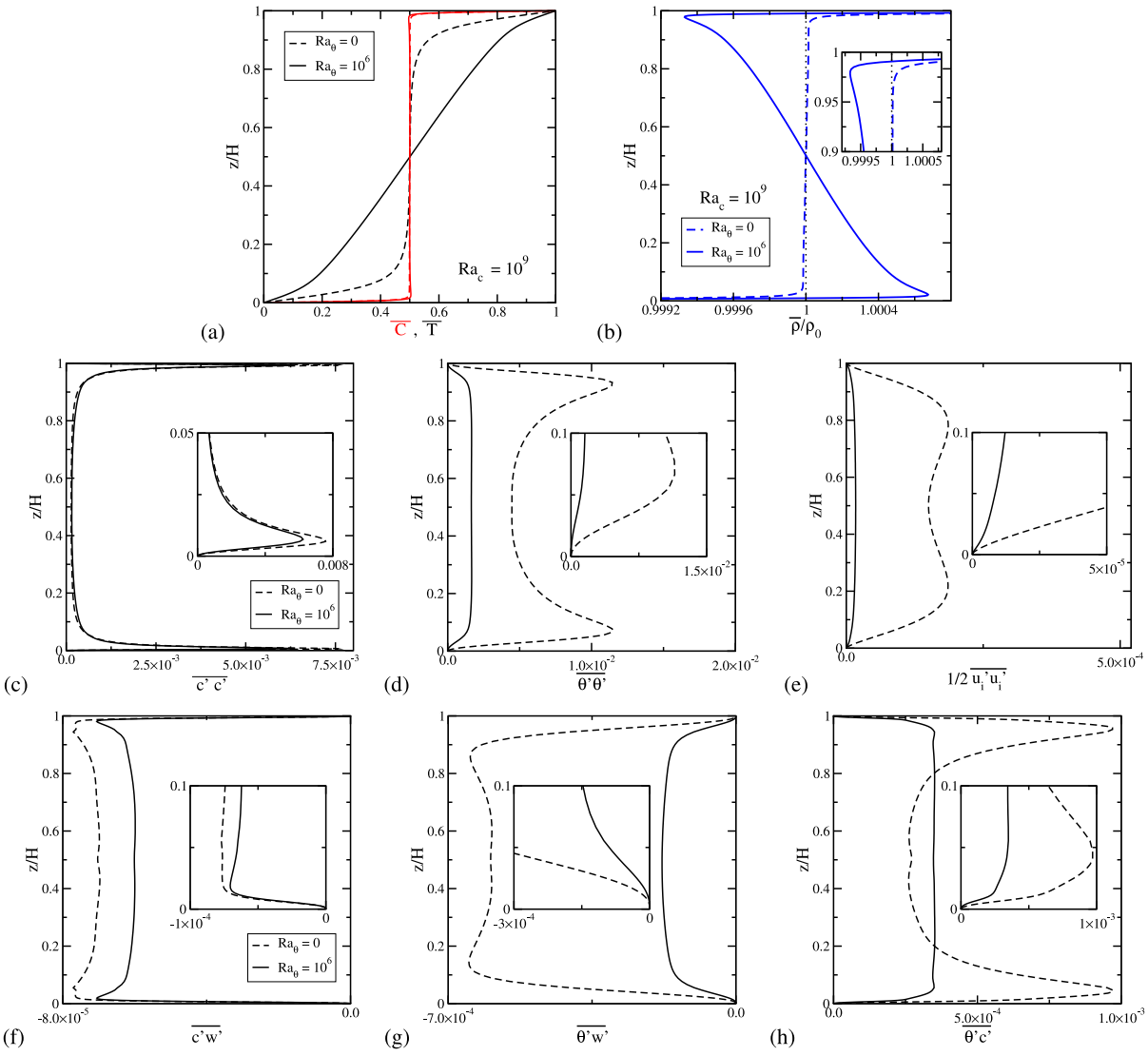

Fig. 9. Same as in previous figure only now for $Ra_c = 10^9$.

studies of Yang et al. (2016a). The temperature contours show a well established vertical stratification with imprints of small waves in the horizontal direction in the central part of the domain, Fig. 2(d).

Additional insights are obtained by plotting the concentration contours in three characteristic horizontal planes at z/H = 0.1, 0.5 and 0.9, as shown in Fig. 3. In planes near the walls, a fine network of planform structures with superimposed imprints of the concentration updrafts and downdrafts can be observed. Distinct polygonal patterns emerge with an increase in Ra_θ, Fig. 3(b–f). Opposite red/blue patches can be seen, which are associated with corresponding concentration downdrafts/updrafts, respectively. In the central horizontal plane, the planform structures disappear, and a significant increase in the number of concentration plumes is produced at $Ra_\theta = 10^6$ compared to the neutral case, Fig. 3(c–d).

We now move to the high $Ra_c = 10^9$ case, Figs. 4–5. Here we expect weaker effects of the imposed thermal stratification due to a lower density ratio of $\Lambda = 0.1$ compared to $\Lambda = 1$ for $Ra_c = 10^8$ (both at $Ra_\theta = 10^6$). From the vertical cross-sections, we can observe that significantly thinner concentration plumes are generated, Fig. 4(a–b). Despite the lower Λ, there is still a significant impact on the flow structures, Fig. 4(e–f). Similarly, the temperature field again shows the well-defined vertical stratification, Fig. 4(c–d). The horizontal cross-sections reveal a significant increase in the number of concentration plumes, Fig. 5(c–d). The planform structures are again generated near the walls, with typical opposing heavy/light (red/blue) fluid concentration distributions, Fig. 5(a–b,e–f).

3.3. Local instantaneous mass and heat transfer at the wall

Next, we investigate the impact of the observed changes in flow, concentration, and temperature distributions at different Ra_c and Ra_θ on the instantaneous local mass and heat transfer. Contours of the local concentration Nusselt number (Nu_c) (equivalent to the Sherwood number for the mass transfer characterization) at the upper wall are shown in Fig. 6. At lower values of $Ra_c = 10^7$, the impinging locations (where the light fluid impinges on the upper wall) are located in the centres of the cellular-like planform network, Fig. 6(a). Similar structures are also observed at $Ra_c = 10^8$, Fig. 6(b), whereas a less structured organization is present at $Ra_c = 10^9$, Fig. 6(c). Strong thermal stratification ($Ra_\theta = 10^6$) leads to a more dense cellular-like network corresponding to increase of the number of the concentration updrafts that are impinging at the upper wall, Fig. 6(d–e–f). The thickness of the edges of the characteristic cellular structures also reduces with an increase in Ra_c, but is not affected by changes in Ra_θ. Despite this significant spatial reorganization of the local mass transfer patterns at the upper wall, the integral mass transfer remains almost constant

Table 1
An overview of the most important simulations with characteristic non-dimensional parameters and observed regimes.

Ra_c	Ra_θ	Λ	Nu_c	Nu_θ	Regime Observed
10^7	0	0	17.35	1.55	RBC-like
	10^6	10	16.9	1.011	Concentration fingers
10^8	0	0	33.15	3.26	RBC-like
	10^6	1	34.98	1.164	Concentration fingers
10^9	0	0	69.25	7.2	RBC-like
	10^6	0.1	70.15	2.95	Concentration fingers

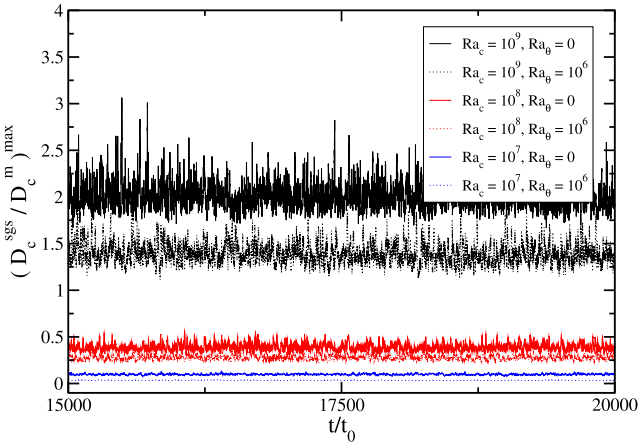

Fig. A.10. The time-evolution of the maximum of the characteristic ratio between the turbulent (sgs) ($D_c^{sgs} = \nu_t^{sgs}/Pr_c^{sgs}$) and molecular ($D_c^m = \nu/Pr_c$) concentration diffusivity for different values of Ra_c and Ra_θ. Here, the non-dimensional time is $t_0 = H/U_0$, and $U_0 = \sqrt{\beta_c g \Delta c H}$.

for both Ra_θ values (recall Fig. 1(a)). Contours of the local thermal Nusselt number at the upper wall show a different spatial organization, Fig. 7. The locations of enhanced local heat transfer coincide with the central parts of the local mass transfer cellular network, but now with distinct circular patterns due to significantly larger diffusion effects (i.e. smaller values of Pr_θ). In contrast to local mass transfer, the spatial reorganization of local heat transfer has a strong impact on the integral heat transfer too, as can be seen from the reported ranges of the Nu_θ values, Fig. 7 as well as from Fig. 1(b). Furthermore, with an increase in Ra_c, the number of distinct regions with locally elevated heat transfer also increases, Fig. 7(d–e–f). An overview of the most important simulations with characteristic non-dimensional parameters and observed regimes is given in Table 1.

3.4. The first- and second-moment correlations

Finally, we examine in detail the distributions of long-term, time-averaged turbulence statistics collected from the cases considered above. The information on the cross-correlation terms of turbulent double-diffusive convection is scarce in the literature. Due to their importance in the development and validation of Reynolds-Averaged Navier–Stokes (RANS) type of turbulence models, we focus on resulting mutual (cross)correlations between velocity, concentration, and temperature fields. Vertical profiles (each vertical point is the result of horizontal spatial averaging) of the time-averaged first- and second-moments are shown in Figs. 8 and 9, for $Ra_c = 10^7$ and 10^9 (i.e. we select the lower and upper range of Ra_c), respectively.

The mean concentration and temperature profiles at $Ra_c = 10^7$ are shown in Fig. 8(a). For the neutral case, the mean concentration profile depicts steep gradients near the walls, and a uniform distribution in the centre of the domain. After imposing strong thermal stratification, the mean concentration profile changes, maintaining steep gradients near the walls while forming a linear shift in the central part of the domain. In contrast, the mean temperature profiles exhibit significantly more diffusive distributions close to the fully thermally conducting state at $Ra_\theta = 10^6$ (as seen in Fig. 1(b)). The vertical profiles of the non-dimensional mean density, calculated as $\overline{\rho}/\rho_0 = 1 + \beta_c\left(\overline{C} - c_0\right) - \beta_\theta\left(\overline{T} - \theta_0\right)$, are shown in Fig. 8(b). For the neutral case, the density profile exhibits a positive gradient near the lower and upper boundaries, while the central part of the domain shows a constant value. At $Ra_\theta = 10^6$, a strong negative gradient is observed in the central part of the domain. These different density profile distributions result from the observed flow regimes: a typical concentration-driven Rayleigh–Bénard convection for the neutral case and distinct concentration finger-like structures for the strong stratification case.

The concentration variance profiles exhibit a double-peak behaviour with approximately constant values in the centre, Fig. 8(c). While the peak values are slightly lower at $Ra_\theta = 10^6$, the central distribution shows a significantly higher contribution compared to the neutral state. In contrast, the temperature variance profiles display a significantly different behaviour, confirming a dissimilarity between turbulence scalars, Fig. 8(d). There is a single peak behaviour for the neutral state, whereas an almost total suppression is obtained at $Ra_\theta = 10^6$. The profiles of the kinetic energy of turbulence also depict a strong suppression, with a single peak in the centre of the domain, as seen in Fig. 8(e). The vertical component of the turbulent concentration flux shows significant contribution in the central part of the domain, followed by strong suppression in the near-wall regions, Fig. 8(f). Here, a 50% reduction is observed in the centre of domain after activation of strong thermal stratification. The vertical component of the turbulent heat flux shows a single peak behaviour for the neutral case, followed by strong suppression at $Ra_\theta = 10^6$, Fig. 8(g). It is interesting to observe that the profiles of the $\overline{\theta' c'}$ correlation show finite values in the centre of the domain, even though the temperature variance is strongly suppressed here at $Ra_\theta = 10^6$, Fig. 8(h).

The mean concentration profiles at $Ra_c = 10^9$ are only slightly affected by changes in Ra_θ, exhibiting very steep distributions in the near-wall regions and a uniform profile in the central part, Fig. 9(a). In contrast, the mean temperature displays greater sensitivity to variations in Ra_θ. For the neutral case, the mean density profile exhibits a positive gradient throughout the entire domain height, including the central part, as shown in Fig. 9(b). At $Ra_\theta = 10^6$, the central part is characterized by a distinct negative gradient, while the mean density gradient remains positive within the near-wall regions.

With an increase in Ra_θ, the profiles of concentration variance show a slight decrease in peak values, followed by a modest increase in the central region, Fig. 9(c). The profiles of temperature variance ($\overline{\theta'\theta'}$), turbulent kinetic energy ($1/2\overline{u_i' u_i'}$), and turbulent heat flux ($\overline{\theta' w'}$), depicted in Fig. 9(d),(e),(g) - all undergo a transition from a double-peak to a single-peak profile with increasing Ra_θ, accompanied by noticeable suppression in the central region. The profiles of the turbulent concentration flux ($\overline{c' w'}$) show smaller changes with characteristic double peak behaviour, Fig. 9(f). Finally, the profiles of the fluctuating temperature/concentration correlation ($\overline{\theta' c'}$) show an interesting behaviour, Fig. 9(h). The double-peak profile present in the neutral case is replaced by a uniform distribution in the central part at $Ra_\theta = 10^6$. Moreover, the peaks are significantly suppressed in the proximity of the upper and lower walls, whereas the values in the central part now surpass the neutral values.

4. Summary and conclusions

We performed a series of numerical simulations to study turbulent double-diffusion, focusing on the interaction between concentration and temperature fields under stable thermal stratifications of varying strengths. We considered a situation where a warmer and saltier layer initially resides above a colder and less salty layer of fluid. In this

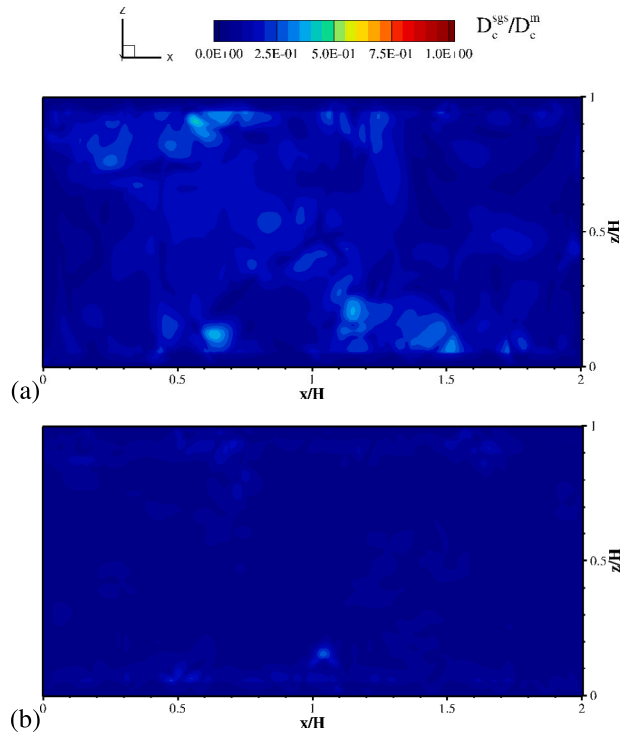

Fig. A.11. Contours of the instantaneous ratio of the turbulent (sgs) ($D_c^{sgs} = \nu_t^{sgs}/Pr_c^{sgs}$) and molecular ($D_c^m = \nu/Pr_c$) concentration diffusivity at $Ra_c = 10^8$, $Ra_\theta = 0$ (a) and $Ra_\theta = 10^6$ (b).

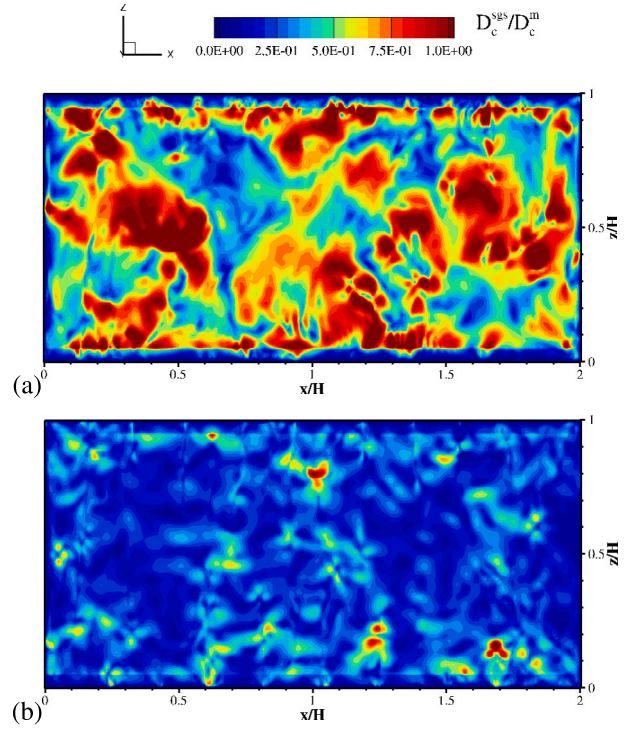

Fig. A.12. Contours of the instantaneous ratio of the turbulent (sgs) ($D_c^{sgs} = \nu_t^{sgs}/Pr_c^{sgs}$) and molecular ($D_c^m = \nu/Pr_c$) concentration diffusivity at $Ra_c = 10^9$, $Ra_\theta = 0$ (a) and $Ra_\theta = 10^6$ (b).

setup, the concentration gradient initiates mixing (unstable concentration stratification), while the temperature gradient tends to stabilize the flow. The present results obtained using well-resolved LES showed good agreement with fully resolving DNS from the literature over the entire range of parameters considered. Because of the formation of the concentration finger structures, the imposed stable thermal stratification slightly increased the total mass transfer compared to the neutral situation (i.e. when temperature acts as a passive scalar). In contrast, the total heat transfer is significantly reduced when strong thermal stratification is imposed. The local mass and heat transfer along the active boundaries exhibit strong sensitivity to the imposed thermal stratification, leading to the formation of cellular-like networks for the concentration and circular imprints for the temperature field.

Finally, the vertical profiles of the long-term time-averaged first and second moments reveal various degree of sensitivity to the imposed thermal stratification. At a smaller value of $Ra_c = 10^7$, the temperature variance, turbulent heat flux, and turbulent kinetic energy are greatly suppressed, while the concentration variance is only slightly affected. At higher values of $Ra_c = 10^9$, the concentration variance shows marginal differences, whereas the remaining correlations exhibit suppression trends, with the exception of $\overline{\theta' c'}$, which is enhanced in the central part of the domain compared to the neutral case. The presented distributions of the second-moments can be used for further development, validation, and testing of the RANS-type turbulence models for double-diffusive convection phenomena.

CRediT authorship contribution statement

S. Kenjereš: Writing – review & editing, Writing – original draft, Visualization, Validation, Supervision, Software, Resources, Methodology, Investigation, Formal analysis, Data curation, Conceptualization. **R. Roovers:** Writing – original draft, Validation, Software, Methodology, Investigation, Formal analysis, Data curation.

Declaration of competing interest

The authors declare that they have no known competing financial interests or personal relationships that could have appeared to influence the work reported in this paper.

Acknowledgement

The authors acknowledge the use of computational resources of the DelftBlue supercomputer, provided by Delft High Performance Computing Centre (https://www.tudelft.nl/dhpc).

Appendix

See Figs. A.10–A.12.

Data availability

Data will be made available on request.

References

Celik, I., Cehreli, Z., Yavuz, I., 2005. Index of resolution quality for large eddy simulations. J. Fluids Eng. 127, 949–958.

Chakkingal, M., Voigt, R., Kleijn, C., Kenjereš, S., 2020. Effect of double-diffusive convection with cross gradients on heat and mass transfer in a cubical enclosure with adiabatic cylindrical obstacles. Int. J. Heat Fluid Flow 83, 108574, 1–11.

Eidson, T., 1984. Numerical simulation of the turbulent Rayleigh-Bénard problem using subgrid modelling. J. Fluid Mech. 158, 245–268.

Ferziger, J., Perić, M., Street, R., 2019. Computational Methods for Fluid Dynamics. http://dx.doi.org/10.1007/978-3-319-99693-6.

Grossmann, G., Lohse, D., 2000. Scaling in thermal convection: a unifying theory. J. Fluid Mech. 407, 27–56.

Hage, E., Tilgner, A., 2010. High Rayleigh number convection with double diffusive fingers. Phys. Fluids 22, 076603, 1–7.

Hanjalić, K., Musemić, R., 1997. Modeling the dynamics of double-diffusive scalar fields at various stability conditions. Int. J. Heat Fluid Flow 18, 360–367.
Huppert, H., Turner, J., 1981. Double-diffusive convection. J. Fluid Mech. 106, 299–329.
Kellner, M., Tilgner, A., 2014. Transition to finger convection in double-diffusive convection. Phys. Fluids 26, 004103, 1–10.
Kenjereš, S., 2008. Electromagnetic enhancements of turbulent heat transfer. Phys. Rev. E 78, 066309. http://dx.doi.org/10.1103/PhysRevE.78.066309, 1–5.
Kenjereš, S., 2009. Large-eddy simulations of targeted electromagnetic control of buoyancy driven turbulent flow in a slender cavity. Theor. Comput. Fluid Dyn. 23, 471–489. http://dx.doi.org/10.1007/s00162-009-0124-7.
Kenjereš, S., 2011. Electromagnetically driven dwarf tornados in turbulent convection. Phys. Fluids 23 (015103), 1–10. http://dx.doi.org/10.1063/1.3541817.
Kenjereš, S., 2015. Heat transfer enhancement induced by wall inclination in turbulent thermal convection. Phys. Rev. E 92 (053006), 1–14. http://dx.doi.org/10.1103/PhysRevE.92.053006.
Kenjereš, S., Hanjalić, K., 2002. Numerical insight into flow structure in ultraturbulent thermal convection. Phys. Rev. E 66, 036307, 1–5.
Kenjereš, S., Hanjalić, K., 2004. Numerical simulation of magnetic control of heat transfer in thermal convection. Int. J. Heat Fluid Flow 25, 559–568. http://dx.doi.org/10.1016/j.ijheatfluidflow.2004.02.021.
Kenjereš, S., Hanjalić, K., 2006. LES, T-RANS and hybrid simulations of thermal convection at high ra numbers. Int. J. Heat Fluid Flow 27, 800–810. http://dx.doi.org/10.1016/j.ijheatfluidflow.2006.03.008.
Mejia, J., Sadiki, A., Molina, A., Chejne, F., Pantangi, P., 2015. Large eddy simulation of the mixing of a passive scalar in a high-Schmidt turbulent jet. J. Fluids Eng. 137 (3), 031301. http://dx.doi.org/10.1115/1.4029224, 1–11.
Ostilla-Mónico, R., Yang, Y., van der Poel, E., Lohse, D., Verzicco, R., 2015. A multiple resolutions strategy for direct numerical simulation of scalar turbulence. J. Comput. Phys. 301, 308–321.
Patankar, S., 1980. Numerical heat transfer and fluid flow. Taylor Francis.
Rosenthal, A., Lüdemann, K., Tilgner, A., 2022. Staircase formation in unstably stratified double diffusive finger convection. Phys. Fluids 34, 116605, 1–10.
Stone, H., 1968. Iterative solution of implicit approximations of multidimensional partial differential equations. SIAM J. Numer. Anal. 5 (3), 530–538.
Turner, J., 1974. Double-diffusive phenomena. Annu. Rev. Fluid Mech. 6 (1), 37–56.
Turner, J., 1985. Multicomponent convection. Annu. Rev. Fluid Mech. 17 (1), 11–44.
Vreman, A., 2004. An eddy-viscosity subgrid-scale model for turbulent shear flow: Algebraic theory and applications. Phys. Fluids 16, 3670–3681.
Yang, T., van der Poel, E., Ostilla-Mónico, R., Sun, C., Verzicco, R., Grossmann, S., Lohse, D., 2015. Salinity transfer in bounded double diffusive convection. J. Fluid Mech. 768, 476–491.
Yang, T., Verzicco, R., Lohse, D., 2016a. Scaling laws and flow structures of double diffusive convection in the finger regime. J. Fluid Mech. 802, 667–689.
Yang, T., Verzicco, R., Lohse, D., 2016b. From convection rolls to finger convection in double-diffusive turbulence. Proc. Natl. Acad. Sci. USA 113 (1), 69–73.
Zaussinger, F., Kupka, F., 2019. Layer formation in double-diffusive convection over resting and moving heated plates. Theor. Comput. Fluid Dyn. 33, 383–409.
Zenklusen, A., Kenjereš, S., Rohr, P., 2016. Mixing at high Schmidt number in a complex porous structure. Chem. Eng. Sci. 150, 74–84.
Zhou, S.-Q., Xia, K.-Q., 2001. Spatially correlated temperature fluctuations in turbulent convection. Phys. Rev. E 63, 046308, 1–6.
Zuo, Z., Wang, Y., Hu, Z., Tong, L., Wu, P., Wang, L., 2024. Visualization study on double-diffusive convection during a rollover in liquid energy storage tanks. J. Energy Storage 76, 109013, 1–12.